

# Spin-orbit interaction driven collective electron-hole excitations in a noncentrosymmetric nodal loop Weyl semimetal

Kyo-Hoon Ahn,<sup>1</sup> Kwan-Woo Lee,<sup>1,2,\*</sup> and Warren E. Pickett<sup>3,†</sup>

<sup>1</sup>Department of Applied Physics, Graduate School, Korea University, Sejong 339-700, Korea

<sup>2</sup>Department of Display and Semiconductor Physics, Korea University, Sejong 339-700, Korea

<sup>3</sup>Department of Physics, University of California, Davis, California 95616, USA

(Received 13 July 2015; published 28 September 2015)

NbP is one member of a new class of nodal loop semimetals characterized by the cooperative effects of spin-orbit coupling (SOC) and a lack of inversion center. Here transport and spectroscopic properties of NbP are evaluated using density functional theory methods. SOC together with the lack of inversion symmetry splits degeneracies, giving rise to “Russian doll nested” Fermi surfaces containing  $4 \times 10^{-4}$  electron (hole) carriers/f.u. Due to the modest SOC strength in Nb, the Fermi surfaces map out the Weyl nodal loops. Calculated structure around  $T^* \approx 100$  K in transport properties reproduces well the observed transport behavior only when SOC is included, attesting to the precision of the (delicate) calculations and the stoichiometry of the samples. Low-energy collective electron-hole excitations (plasmons) in the 20–60 meV range result from the nodal loop splitting.

DOI: 10.1103/PhysRevB.92.115149

PACS number(s): 72.15.Eb, 78.20.Ci, 71.20.Be, 71.18.+y

## I. INTRODUCTION

Weyl semimetals (WSs) have Weyl points, comprised of a linear crossing of valence and conduction bands [1] near the Fermi energy  $E_F$ . WSs can be realized from a lack of time-reversal symmetry (magnetic ordering, or applied field  $B$ ) [1–3], or from no inversion symmetry in three-dimensional compounds [4,5], and they show peculiar features, such as Fermi arcs from surface states connecting two Weyl points with different chirality [1,4,5]. Experimental evidence has been obtained using x-ray angle-resolved photoemission spectroscopy [6]. Extremely large magnetoresistivity (XMR) also occurs in some WSs, with a recent analysis by Burkov [3] concluding that XMR should be expected in high-mobility semimetals where Weyl or Dirac points lie near the Fermi surface (FS). XMR was observed also in the semimetal WTe<sub>2</sub>, showing unsaturated MR up to 60 T [7], attributed to precise electron and hole carrier compensation, as in Bi and other stoichiometric semimetals.

Recently a “nodal loop” Weyl semimetal phase with potentially distinctive properties has been proposed on theoretical grounds [4,5] in the nonmagnetic noncentrosymmetric isovalent class TaAs, TaP, NbAs, and NbP; its structure is shown in Fig. 1. A previous proposal of nodal loop WSs by Phillips and Aji invoked time-reversal symmetry breaking [8] rather than the lack of inversion symmetry of this class of pnictides. Since these suggestions, XMR has been observed in both TaAs [9,10] and NbP [10,11]. NbP, upon which we focus here, shows XMR of 8500 at 2 K for  $B = 9$  T, increasing to  $3 \times 10^4$  at 4 K at  $B = 30$  T, to  $10^5$  at 60 T, and remains unsaturated [11]. These colossal XMR values reflect the excellent conduction at low temperatures, with resistivity as low as  $0.1 \mu\Omega \text{ cm}$ , and a metal-to-insulator crossover with field at 100 K and below. A high-mobility  $\mu = 5 \times 10^6 \text{ cm}^2/\text{V s}$  and low carrier density of  $1.5 \times 10^{18} \text{ cm}^{-3}$  at low  $T$  was inferred from the conventional single band expressions, which,

however, are not quantitative for multiband semimetals. As temperature increases, the Hall coefficient  $R_H$  changes sign from electronlike to holelike, and the mobility rapidly changes in the 50–150 K range, correlating with the metal-to-insulator crossover. A multiband model and additional data will be necessary to sort out individual carrier densities and mobilities. NbP has the smallest spin-orbit coupling (SOC) of this class, making it the most delicate example of the features of nodal loop WSs.

From both theoretical and experimental viewpoints, nodal loop semimetals comprise a new class of materials with topological behavior. In this paper, we focus on effects of SOC on their electronic properties and evaluate the optical and transport coefficients of NbP, using density functional theory based methods that enable a direct theory-experiment comparison. A central feature that emerges is electronic fine structure driven by the combination of SOC and lack of an inversion center, a feature elaborated on by Samokhin [12] from a model viewpoint. This splitting in a semimetal with small closed Fermi surfaces (FSs) results in a “Russian doll nested” pair of FSs, and new low-energy interband transition strength pilfered from the Drude strength by noncentrosymmetry. The FS character is clarified, and low-energy collective electronic excitations (plasmons) arising from the electronic fine structure are predicted. While plasmons have been studied in conventional WSs [13–16], their appearance in nodal loop WSs as well as several other properties discussed here are distinctive when the special “nodal loop semimetal” character is encountered.

## II. STRUCTURE AND THEORETICAL METHODS

As shown in Fig. 1, NbP has a body-centered-tetragonal lattice of the space group  $I4_1md$  (no. 109) [17]. This space group has  $4mm$  point group, is nonsymmorphic, and (importantly) lacks inversion symmetry. The structure can be pictured as columns of face-shared NbP<sub>6</sub> trigonal prisms oriented along the  $\hat{a}$  axis, edge-shared along the  $\hat{b}$  axis in one layer. The trigonal columns are  $90^\circ$  rotated in the next

\*mckwan@korea.ac.kr

†pickett@physics.ucdavis.edu

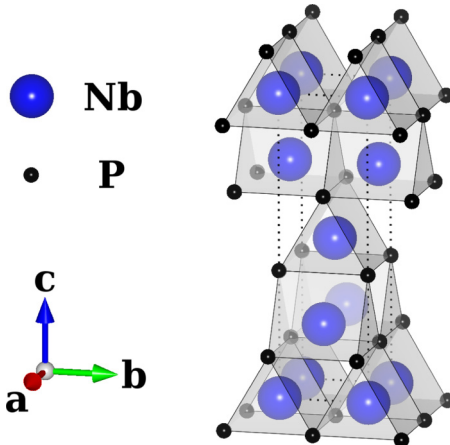


FIG. 1. (Color online) Body-centered-tetragonal  $I4_1md$  structure of NbP. It consists of edge-sharing  $NbP_6$  trigonal prisms, which are  $90^\circ$  rotated in the next layer. The lack of inversion symmetry is evident: the prisms all “point” upward.

layer along the  $\hat{c}$  axis, giving overall tetragonal symmetry. In the structure with the experiment lattice parameters [17] of  $a = 3.3324 \text{ \AA}$  and  $c = 11.3705 \text{ \AA}$ , both Nb and P ions lie at  $4a$  positions  $(0,0,z)$ :  $z_{\text{Nb}} = 0$ ,  $z_{\text{P}} = 0.4176$ ; the site symmetry is  $2mm$ . Our optimized positions using the generalized gradient approximation (GGA) with the Perdew-Burke-Ernzerhof (PBE) exchange-correlation functional [18] in FPLO [19] coincided with the experimental values. This structure leads to nearly identical Nb-P bond lengths of  $2.53 \pm 0.01 \text{ \AA}$  and P-Nb-P bond angles around  $82^\circ$ .

Calculations with the experimental structure were performed using the all-electron full-potential code WIEN2K [20], with selected results confirmed with FPLO. All results are based on the PBE-GGA exchange-correlation functional. One objective is to determine the combined effects of SOC and the lack of inversion center, since delicate features around  $E_F$  are sensitive to SOC and become important.

Calculation of optical properties including SOC is available in WIEN2K [21]. The dielectric function  $\epsilon_{ij}(\omega)$ , with only diagonal  $\epsilon_{aa} = \epsilon_{bb}$  and  $\epsilon_{cc}$  components due to tetragonal symmetry, is decomposed into intra- and interband contributions. The imaginary parts of each contribution are given by [21,22]

$$\begin{aligned} \text{Im}\epsilon_{jj}^{\text{intra}}(\omega) &\propto \frac{\Gamma\Omega_{p,jj}^2}{\omega(\omega^2 + \Gamma^2)}, \\ \text{Im}\epsilon_{jj}^{\text{inter}}(\omega) &\propto \sum_{c,v} \int d\vec{k} \frac{|\langle c_{\vec{k}} | p_j | v_{\vec{k}} \rangle|^2}{\omega^2} \delta(\varepsilon_{c_{\vec{k}}} - \varepsilon_{v_{\vec{k}}} - \omega), \quad (1) \end{aligned}$$

where  $\vec{p}$  is the momentum operator, and  $\varepsilon_{c_{\vec{k}}}$  and  $\varepsilon_{v_{\vec{k}}}$  are energies of the occupied  $v_{\vec{k}}$  and unoccupied  $c_{\vec{k}}$  orbitals, respectively. In the intraband term, which contains the Drude divergence for  $\omega \rightarrow 0$ ,  $\Omega_{p,jj}$  is the Drude plasma frequency and  $\Gamma$  (chosen to be 10 meV here) is an inverse scattering lifetime  $\tau$ . The corresponding real parts are obtained by the Kramers-Kronig relation.

The transport calculations were carried out using semiclassical Bloch-Boltzmann transport theory, implemented in the BOLTZTRAP code [23] that is interfaced to WIEN2K. No approximations beyond the constant scattering time approximation

are made. In all calculations performed here, the Brillouin zone was sampled with a dense  $k$ -mesh up to  $60 \times 60 \times 60$  to treat the semimetallic fine structure carefully. In WIEN2K, the basis size was determined by  $R_{\text{mt}} K_{\text{max}} = 8$ , and augmented plane-wave sphere radii of 2.5 Bohr (Nb) and 2.14 Bohr (P) were used.

### III. RESULTS

#### A. Electronic fine structure

We first address the electronic structure obtained with fine  $k$ -point and energy meshes. Figure 2 shows the GGA and GGA+SOC band structures near  $E_F$ . Semimetallic character with a band crossing along at least three symmetry directions appears, with valence-conduction overlaps mostly of the order of 150 meV. This band behavior leads to a pseudogap centered 20 meV below  $E_F$  (Fig. 2), with a very small density of states (DOS)  $N(E_F) = 0.046$  states/eV per f.u. While these results are similar to the previous report [4,11], we examine the origins and consequences more completely.

Inclusion of SOC leads to unconventional consequences. As usual, SOC converts many band crossings along symmetry lines into anticrossings; here gapping bands by a few tens of meV near  $E_F$ . However, the lack of inversion symmetry leads to lifting of band degeneracy over entire symmetry planes [4], with splittings in the 20–200 meV range. In spite of the modest magnitude of SOC in  $4d$  Nb, SOC will play an important role in determining both the thermal and spectroscopic properties of NbP.

#### B. Fermi surfaces

The FSs obtained from GGA+SOC are displayed in Fig. 3; see the caption for a description. They are similar to those presented earlier, but they are displayed in an extended zone manner to illustrate their toroidal origin. Weng *et al.* have described in detail [4] the underlying features of the Weyl

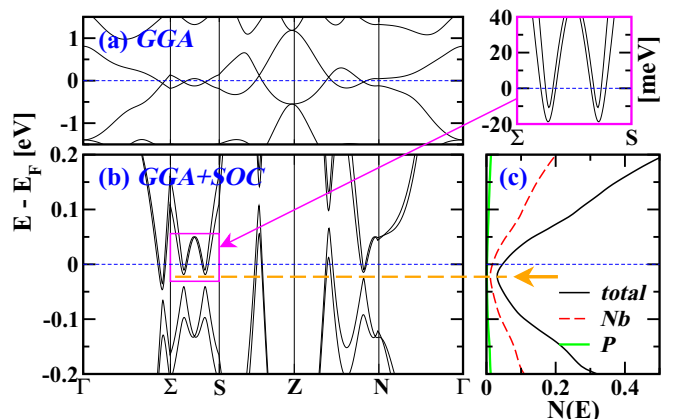


FIG. 2. (Color online) (a) GGA bands in the range of  $-1.5$  to  $1.5$  eV and (b) GGA+SOC bands in the range of  $-0.2$  to  $0.2$  eV, with  $E_F$  set to zero. The symmetry points can be identified in Fig. 3. The upper right panel enlargement shows the splitting by  $\sim 10$  meV of bands by SOC in this noncentrosymmetric structure. (c) Density of states (GGA+SOC) showing the pseudogap centered 20 meV below  $E_F$ .

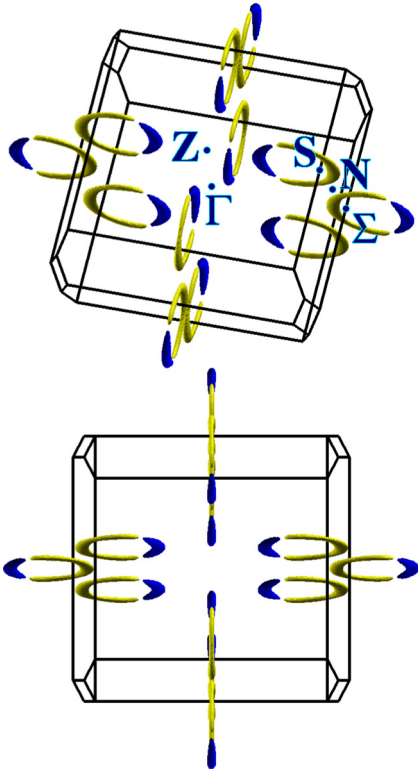


FIG. 3. (Color online) NbP Fermi surfaces (FSs) including SOC and shown from two angles, the lower one viewed along the  $k_x$  axis to reveal the thinness of the surfaces in the mirror planes. The extended zone representation makes the toroidal origin of the FSs evident. The hole (blue) boomerang FSs form bent and “sharply” tipped boomerang surfaces, the electron (yellow) new moon surfaces are similar but extend over a larger angle of the torus.

nature of NbP and isovalent partner compounds. Without SOC, mirror symmetry protected nodal loops lie precisely in the mirror planes  $k_x = 0$  and  $k_y = 0$ . The nodal loops consist of band degeneracies  $\varepsilon_{1,s}(\vec{k}) = \varepsilon_{2,s}(\vec{k})$  ( $s$  is spin degeneracy). The locus of  $\vec{k}$  points at this intersection forms the ring in the  $\Gamma$ -ZN mirror plane, not at constant energy but, for these compounds, in a small energy range including  $E_F$ . The FS intersects the nodal loop, so it must include an even number of doubly degenerate *Fermi points* where  $\varepsilon_{1,s}(\vec{k}) = \varepsilon_{2,s}(\vec{k}) = E_F$ . Such nodal loops have also been found in two-dimensional SrVO<sub>3</sub> nanolayers [24].

In this noncentrosymmetric structure, SOC splits the bands forming the nodal loops, leaving two symmetry-inequivalent pairs of Weyl points (12 in all) near but not on the FSs, the points being provided explicitly by Weng *et al.* [4]. One lies in the  $k_z = 0$  plane, the other at a general  $\vec{k}$  point lying near the  $\Gamma$ -NZ plane. The band splitting is highly anisotropic; each FS (Fig. 3) consists of a flattened torus (annulus) pinched off into one “boomerang” containing holes and one “new moon” containing electrons. Small doping will alter the position of the pinching, hence changing the number of electron and hole carriers.

For a stoichiometric compound, the FSs contain an equal number of holes and electrons, and from calculated band fillings we obtain  $4.2 \times 10^{-4}$  electron (hole) carriers per f.u.

This value corresponds to high-velocity carriers of each sign separated on average by 13 lattice constants in each direction. The rms Fermi velocities are  $v_{F,aa} = 3.7$ ,  $v_{F,cc} = 1.6$ , in  $10^7$  cm/s, a factor of 2.35 in anisotropy. Note that the velocities are typical of *metallic* compounds, not semimetals, due to the dispersive bands crossing  $E_F$ , i.e., the Weyl character (analogous to graphene). For the Drude plasma energy, the semimetallic value of  $N(E_F)$  but normal metal velocities lead to  $\Omega_{p,aa} = 1.0$  eV,  $\Omega_{p,cc} = 0.4$  eV.

What cannot be seen in Fig. 3 is the doubling of the FSs resulting from the interplay of SOC with the noncentrosymmetric crystalline symmetry. With the band degeneracy split, Fermi surfaces become “Russian doll nested” pairs, one inside the other. This band-splitting effect has been discussed for Pt-based superconductors [25] and for electronic properties more generally [12]. The band splitting aspect is effective both in  $k$ -space (closely nested Fermi surfaces) and in energy, with consequences discussed below.

### C. Transport properties

Transport behavior in semimetals is very sensitive to Fermiology and to regions of high curvature, but we have found that calculated values based on quasiclassical Bloch-Boltzmann theory agree very well with observed behavior [11]. The Hall tensor components  $R_H(T)$  including SOC, displayed in Fig. 4(a), show a change in sign at  $T_c = 125$  K, precisely where the experimental  $R_H$  changes sign [11]. This change of sign is a strong reminder that in a multiband, compensated semimetal,  $R_H$  bears no direct relation to carrier densities [26].

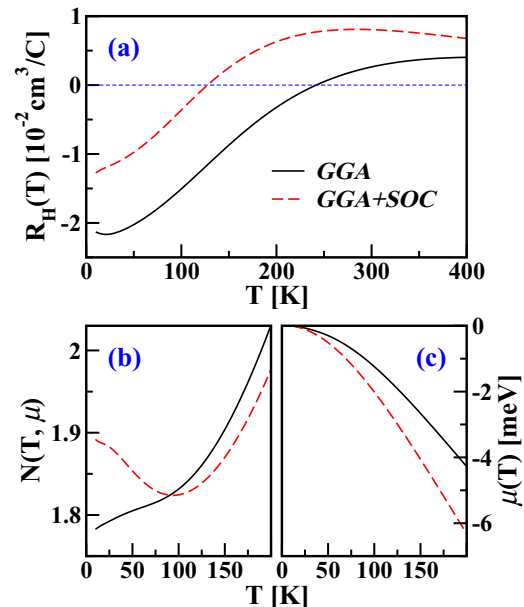


FIG. 4. (Color online) (a) Temperature ( $T$ ) -dependent Hall coefficients  $R_H(T)$  calculated in both GGA and GGA+SOC, which show similar  $T$  dependence but distinctions in the zero crossing temperature;  $T = 125$  K in GGA+SOC, compared to  $T = 230$  K in GGA. (b)  $T$ -dependent total density of states  $N(T, \mu)$  at chemical potential  $\mu(T)$ .  $N(T, \mu)$  shows a minimum around  $T = 100$  K in GGA+SOC, while that of GGA increases with increasing  $T$ . (c)  $\mu(T)$  with respect to  $E_F$  at  $T = 0$  K.

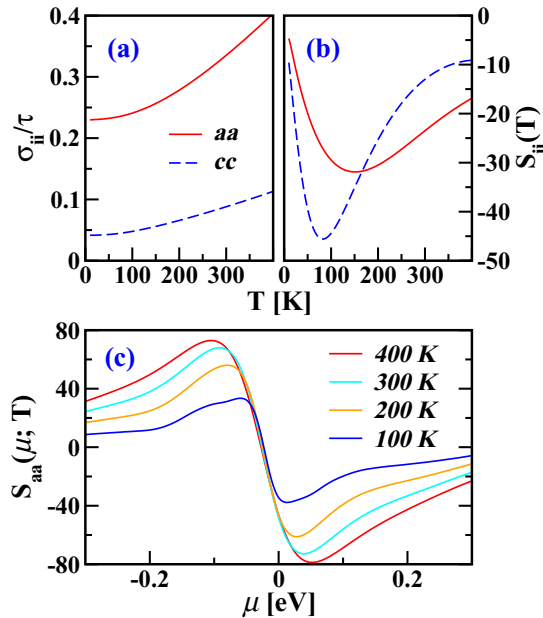


FIG. 5. (Color online) Temperature- and polarization-dependent (a) conductivity tensor over scattering time, in  $10^{20} (\Omega \text{ m s})^{-1}$ , and (b) Seebeck coefficients  $S_{ii}$  ( $\mu\text{V}/\text{cm}$ ); note the minimum in the latter in the 100–150 K range. (c) The Seebeck coefficient  $S_{aa}(\mu; T)$  vs band filling  $\mu$  at various temperatures, within GGA+SOC. The change at very small levels of doping is extremely rapid, reflecting the movement away from charge compensation;  $S_{cc}$  behaves in the same manner. The temperature variation is monotonic.

This statement is particularly true when the FSs are strongly nonellipsoidal and extremely anisotropic.

The experiment-theory agreement reflects not only the precision of the calculations but also the excellent stoichiometry of the samples; the stoichiometry could not be established precisely but is supported also by the high mobility. The magnitude of  $R_H(T)$  around 250 K is within a factor of 2 of the experimental value. This is really excellent agreement, because of the compensating contributions from small electron and hole surfaces, which have regions of large curvature. The expression for  $R_H$  in Bloch-Boltzmann theory has the interpretation of giving it as the average of the curvature over the FSs. A strong temperature dependence and a likely change of sign with temperature should be anticipated in nodal loop WSSs. The experimental  $R_H$  becomes at the lowest temperature two orders of magnitude larger in magnitude than our calculated value, and it is clear from the “pointed” FSs in Fig. 3 that evaluating  $R_H$  (which as mentioned is an average of the FS curvature) at  $T = 0$  is a substantial numerical challenge.

The chemical potential  $\mu(T)$ , displayed in Fig. 4(c), decreases with increasing  $T$  reflecting the strong differences in the electron and hole densities of states. This variation is different in sign from another XMR compound WTe<sub>2</sub> [27], reflecting different DOSs of the valence and conduction bands of the two compounds. The DOS at the chemical potential  $N(\mu)$ , shown in Fig. 4(b), is reduced and achieves a minimum around 100 K before turning around. Figure 5(a) displays the conductivity tensor components  $\sigma_{ii}/\tau$ , which incorporates the anisotropy of  $\Omega_{p,jj}$ , which is about five times larger in-plane.

The  $T$ -dependent Seebeck coefficients, shown in Fig. 5(b), have net *n*-type sign. They peak (in magnitude) at 100–150 K before again becoming small. The dependence on chemical potential  $\mu$ , which can be varied by doping or by gating, is extremely strong near stoichiometry [see Fig. 4(c)]. The near-perfect cancellation of electron and hole contributions (it is perfect  $S_{jj} = 0$  for  $\mu \approx -15$  meV) at stoichiometry is destroyed, with a maximum of  $|S(\mu)|$  being attained around 0.5% hole doping, or half of that for electron doping. The sensitivity makes the thermopower an important gauge of the degree of stoichiometry of samples, which otherwise can be very difficult to determine at this low level.

#### D. Optical properties

The band splitting induced by SOC and the lack of inversion symmetry have qualitative consequences for the optical properties. In conventional WSSs, where Fermi surfaces are simple and model band structures work well, the dielectric response and plasmon signatures of chirality have been well studied [13–16]. Nodal loop WSSs bring new processes to the low-energy, small- $q$  dielectric response. They are compensated semimetals thus providing itinerant electron and hole gases. They are qualitatively different from other semimetals (including conventional WSSs) by having highly nonparabolic and extended Fermi surfaces, and of course by having very closely nested Fermi surfaces. New dielectric phenomena must emerge.

Without either SOC or inversion symmetry breaking, bands are doubly degenerate and contribute accordingly to the intraband Drude response. In nodal loop WSSs, half of this weight is transferred to finite- $q$ , finite- $\omega$  response. The changes will be appreciable only at small energies, and they should involve new response at very small  $q$  wave vectors that connect the finely nested Fermi surfaces, which are on the order of  $10^{-2}\pi/a$ . The Drude response will be relatively unchanged

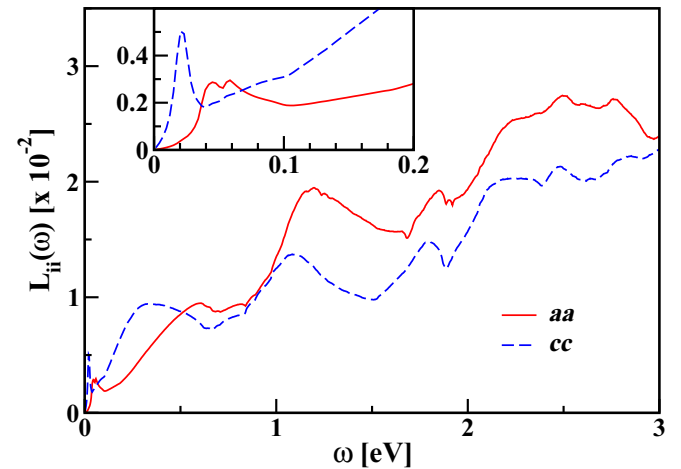


FIG. 6. (Color online) The polarization-dependent energy loss function for NbP assuming a scattering rate  $\Gamma = \hbar/\tau$  of 10 meV. Inset: the  $\hat{c}$ -axis plasmon at 20 meV bifurcates into a pair of plasmons at 40 and 60 meV for in-plane polarization. Above 0.2 eV, the loss function is not greatly anisotropic and is insensitive to  $\Gamma$ .

apart from the factor of 2 reduction in weight, but it may be smeared into the new small- $\omega$ , small- $q$  structures.

The energy loss function, shown in Fig. 6 with scattering rate  $\Gamma = 10$  meV, displays low-energy plasmons when SOC is included, at 20 meV for  $\hat{c}$ -axis polarization and double in-plane plasmon peaks at 40 and 60 meV. The strength of these peaks, and to some degree their positions, are dependent on the presumed scattering rate  $\Gamma$ . The anisotropy we calculate at low energy, based on the strong anisotropy of the Fermi surfaces, may be consistent with the angle dependence of the MR measurements [11]. Given the reported high mobility, the plasmon peaks may be much sharper at low temperature than calculated here. The peaks can be expected also to have temperature dependence, because the varying  $\mu(T)$  induces changes and  $\Gamma$  will be  $T$ -dependent as well. Above 200 meV, we do not expect significant  $T$  dependence of the spectral behavior. Far-infrared spectroscopy may reveal unusual behavior as temperature, field, polarization, and carrier density are varied and tuned.

#### IV. DISCUSSION AND SUMMARY

Our study has illuminated the origins of the unusual and delicate Fermi surfaces of NbP. Without consideration of SOC, the electronic structure includes nodal loops [4] lying in the mirror planes that lead to point Fermi surfaces as well as small electron and hole pockets. In this noncentrosymmetric

structure, SOC removes the spin degeneracy, resulting in Russian doll nested pairs of Fermi surfaces with a pinched-off annulus topology, with electron surfaces converting to hole surfaces across the pinch. The resulting electronic fine structure accounts well for the change in sign of the Hall coefficient at 100 K, which is also the temperature range in which the magnetoresistance begins to grow in size. These features identify 10 meV as a relevant energy scale.

The unusual Fermi surface also accounts for the lack of universal scaling of XMR in NbP and TaP; SOC is much larger in TaP and the Fermi surfaces are sensitive to this. Finally, the fine structure in NbP results in the appearance of polarization-dependent low-energy plasmons in the 20–60 meV range. This study substantially broadens the understanding of how WS behavior impacts the physical properties of NbP, which should also apply in similar form to NbAs, TaP, and TaAs.

#### ACKNOWLEDGMENTS

We acknowledge J.-G. Hong for useful communications on magnetoresistance, and A. S. Botana for useful discussion on calculations in BOLTZTRAP. This research was supported by National Research Foundation of Korea Grant No. NRF-2013R1A1A2A10008946 (K.H.A and K.W.L), by U.S. National Science Foundation Grant No. DMR-1207622-0 (K.W.L.), and by U.S. Department of Energy Grant No. DE-FG02-04ER46111 (W.E.P.).

- 
- [1] X. Wan, A. M. Turner, A. Vishwanath, and S. Y. Savrasov, Topological semimetal and Fermi-arc surface states in the electronic structure of pyrochlore iridates, *Phys. Rev. B* **83**, 205101 (2011).
  - [2] G. Xu, H. Weng, Z. Wang, X. Dai, and Z. Fang, Chern semimetal and the quantized anomalous Hall effect in  $HgCr_2Se_4$ , *Phys. Rev. Lett.* **107**, 186806 (2011).
  - [3] A. A. Burkov, Chiral anomaly and transport in Weyl metals, *J. Phys. Condens. Matter* **27**, 113201 (2015).
  - [4] H. Weng, C. Fang, Z. Fang, B. A. Bernevig, and X. Dai, Weyl semimetal phase in non-centrosymmetric transition-metal monophosphides, *Phys. Rev. X* **5**, 011029 (2015).
  - [5] S.-M. Huang, S.-Y. Xu, I. Belopolski, C.-C. Lee, G. Chang, B. K. Wang, N. Alidoust, G. Bian, M. Neupane, C. Zhang, S. Jia, A. Bansil, H. Lin, and M. Z. Hasan, A Weyl fermion semimetal with surface Fermi arcs in the transition metal monopnictide TaAs class, *Nat. Commun.* **6**, 7373 (2015).
  - [6] B. Q. Lv, N. Xu, H. M. Weng, J. Z. Ma, P. Richard, X. C. Huang, L. X. Zhao, G. F. Chen, C. Matt, F. Bisti, V. Strokov, J. Mesot, Z. Fang, X. Dai, T. Qian, M. Shi, and H. Ding, Observation of Weyl nodes in TaAs, *Nat. Phys.* **11**, 724 (2015).
  - [7] M. N. Ali, J. Xiong, S. Flynn, J. Tao, Q. D. Gibson, L. M. Schoop, T. Liang, N. Haldolaarachchige, M. Hirschberger, N. P. Ong, and R. J. Cava, Large, non-saturating magnetoresistance in  $WTe_2$ , *Nature (London)* **514**, 205 (2014).
  - [8] M. Phillips and V. Aji, Tunable line node semimetals, *Phys. Rev. B* **90**, 115111 (2014).
  - [9] C. Zhang, Z. Yuan, S. Xu, Z. Lin, B. Tong, M. Z. Hasan, J. Wang, C. Zhang, and S. Jia, Tantalum monoarsenide: An exotic compensated semimetal, *arXiv:1502.00251*.
  - [10] C. Zhang, C. Guo, H. Lu, X. Zhang, Z. Yuan, Z. Lin, J. Wang, and S. Jia, Large magnetoresistance over an extended temperature regime in monophosphides of tantalum and niobium, *Phys. Rev. B* **92**, 041203(R) (2015).
  - [11] C. Shekhar, A. K. Nayak, Y. Sun, M. Schmidt, M. Nicklas, I. Leermakers, U. Zeitler, W. Schnelle, J. Grin, C. Felser, and B. Yan, Extremely large magnetoresistance and ultrahigh mobility in the topological Weyl semimetal candidate NbP, *Nat. Phys.* **11**, 645 (2015).
  - [12] K. V. Samokhin, Spin-orbit coupling and semiclassical electron dynamics in noncentrosymmetric metals, *Ann. Phys. (N.Y.)* **324**, 2385 (2009).
  - [13] M. Lv and S.-C. Zhang, Dielectric function, Friedel oscillation, and plasmons in Weyl semimetals, *Int. J. Mod. Phys. B* **27**, 1350177 (2013).
  - [14] I. Panfilov, A. A. Burkov, and D. A. Pesin, Density response in Weyl metals, *Phys. Rev. B* **89**, 245103 (2014).
  - [15] J. Zhou, H.-R. Chang, and D. Xiao, Plasmon mode as a detection of the chiral anomaly in Weyl semimetals, *Phys. Rev. B* **91**, 035114 (2015).
  - [16] J. Hofmann and S. Das Sarma, Plasmon signature in Dirac-Weyl liquids, *Phys. Rev. B* **91**, 241108 (2015).
  - [17] J. Xu, M. Greenblatt, T. Emge, P. Höhn, T. Hughbanks, and Y. Tian, Crystal structure, electric transport, and magnetic properties of niobium monophosphide, *Inorg. Chem.* **35**, 845 (1996).
  - [18] J. P. Perdew, K. Burke, and M. Ernzerhof, Generalized gradient approximation made simple, *Phys. Rev. Lett.* **77**, 3865 (1996).

- [19] K. Koepernik and H. Eschrig, Full-potential nonorthogonal local-orbital minimum-basis band-structure scheme, *Phys. Rev. B* **59**, 1743 (1999).
- [20] K. Schwarz and P. Blaha, Solid state calculations using WIEN2k, *Comput. Mater. Sci.* **28**, 259 (2003).
- [21] C. Ambrosch-Draxl and J. O. Sofo, Linear optical properties of solids within the full-potential linearized augmented plane wave method, *Comput. Phys. Commun.* **175**, 1 (2006).
- [22] Y. Li, K. Foyevtsova, H. O. Jeschke, and R. Valentí, Analysis of the optical conductivity for  $A_2\text{IrO}_3$ ( $A = \text{Na, Li}$ ) from first principles, *Phys. Rev. B* **91**, 161101(R) (2015).
- [23] G. K. H. Madsen and D. J. Singh, BOLTZTRAP. A code for calculating band-structure dependent quantities, *Comput. Phys. Commun.* **175**, 67 (2006).
- [24] V. Pardo and W. E. Pickett, Electron confinement, orbital ordering, and orbital moments in  $d^0$ - $d^1$  oxide heterostructures, *Phys. Rev. B* **81**, 245117 (2010).
- [25] K.-W. Lee and W. E. Pickett, Crystal symmetry, electron-phonon coupling, and superconducting tendencies in  $\text{Li}_2\text{Pd}_3\text{B}$  and  $\text{Li}_2\text{Pt}_3\text{B}$ , *Phys. Rev. B* **72**, 174505 (2005).
- [26] The Hall coefficient does not, however, give a reliable carrier density in a multiband, compensated electron-hole semimetal, as mentioned by Shekhar *et al.* [11].
- [27] Y. Wu, N. H. Jo, M. Ochi, L. Huang, D. Mou, S. L. Bud'ko, P. C. Canfield, N. Trivedi, R. Arita, and A. Kaminski, Temperature induced Lifshitz transition in  $\text{WTe}_2$ , arXiv:1506.03346 [Phys. Rev. Lett. (to be published)].